Spiral Vector Modeling of Brushless Doubly-fed Induction Machines with Short-circuited Rotor Windings

Peng Han[1*], *Ming Cheng*[2], *Zhiwei Zhang*[3] *and Peng Peng*[4]

(1. Ansys, Inc., San Jose, CA 95134, USA;

2. School of Electrical Engineering, Southeast University, Nanjing 210096, China;

3. Department of ECE, The Ohio State University, Columbus, OH 43210, USA;

4. Milwaukee Electric Tool Corporation, Milwaukee, WI 53005, USA)

Abstract: A unified spiral vector model is presented that can be used to assist the finite element method-based performance analysis of brushless doubly-fed induction machines with various short-circuited rotor windings. Specifically, magnet-free brushless doubly-fed induction machines working in doubly-fed or singly-fed synchronous mode are investigated. A dynamic model in spiral vector notation is developed, based on which the torque-angle and power-angle characteristics are derived. It is shown that the investigated brushless machines are equivalent to a traditional non-salient-pole synchronous machine with brushes. By introducing a conversion factor, they can also be analyzed with methods similar to the conventional phasor theory. A comparison is made between the brushless doubly-fed induction machine and non-salient-pole wound-field synchronous machine with brushes, revealing that the performance of the brushless machine degrades faster when the laminated core is saturated. A scaled-down prototype is tested to validate the effectiveness of the theoretical analysis.

Keywords: AC machine, brushless machine, modeling, performance evaluation, synchronous machine

1 Introduction

Doubly-fed machines (DFMs), which feature two independent alternating current (AC) electrical ports (i.e., two accessible AC winding sets) and one common mechanical port (i.e., the shaft), and the synchronous operation functionality, have attracted much attention over recent decades as variable speed motor drives or generators for various applications, such as electric vehicles (EVs) and wind power harvesting [1-2]. The latest research has focused on the brushless counterparts, namely brushless DFMs (BDFMs), for their distinct benefits, including robust construction, no high-cost rare-earth permanent magnets, high reliability, low maintenance cost, and decoupled field and torque control [3-7]. Compared with

brushed DFMs, BDFMs show better potential as a magnet-free option with high reliability for wide-speed-range applications, such as EVs and hybrid EVs.

Modern BDFMs can primarily be categorized into three types: cascaded doubly-fed induction machine (CDFIM), brushless doubly-fed induction machine (BDFIM), and brushless doubly-fed reluctance machine (BDFRM) [8]. Other BDFMs, such as those with a rotary transformer [9], wound rotor [10], and hybrid rotor [11], can be conceived as variants derived from the three main types according to their working principles.

Though bearing quite different topologies, the three BDFMs show strong similarities in steady-state performance, dynamic behavior, and control structure. For several decades, these three BDFMs have been developed in parallel and have stimulated one another; nevertheless, the relationship among these three typical topologies has never been explicitly discussed from the perspective of both design and control, which

is probably due to the differences in their mathematical models.

Among the three main BDFM types, the BDFIM has been well known for its complex construction and dynamic modeling, which can be dated back to the 1990s. A two-axis model in a rotor reference frame was established for the first time for the dynamic simulation [12-14] and stability analysis [15-17] of BDFIMs. A so-called rotor-flux-oriented control scheme was proposed in Ref. [18], which, in fact, formulated the model in two synchronous reference frames. All these models conceptually replace the multiple loops per nest with an equivalent single loop unwarrantedly.

The first two-axis model focusing on the effect of nested loops was proposed in Ref. [19], whereas the technique used for model order reduction lacks theoretical basis. Roberts et al. [20] noticed this problem and normalized the model order reduction process through a matrix method, which was somewhat complicated. A reduced-order unified reference frame *d-q* model of a BDFIM was developed for stator-flux-oriented controller design as well as stability analysis [21-23].

A space vector model with multi-loop circuit equations was also built to provide the most compact version of a BDFIM model without significant loss of accuracy for dynamic performance prediction [24], but this model shows weakness in controller design for specific concerns, such as torque ripple suppression. Direct torque control (DTC) for BDFIMs was proposed for the first time in Ref. [25] and latter investigated in Ref. [26]. Finally, significant performance improvement was achieved by introducing the indirect stator-quantities control concept [27-28].

This study focused on developing a concise unified dynamic mathematical model for BDFIMs with various rotor winding types to facilitate their finite element method-based comparison with the other two main types of BDFMs in the future. Traditionally, the steady-state performance of AC electric machine is analyzed using phasor-based methods, such as phasor equations and phasor diagrams, using complex variables. In contrast, two-axis models, alternatively called *d-q* models, are

mainly used for dynamic analysis and simulations with real variables. Coordinate transformations are required to bridge these two types of analysis. Compared to existing theories, the spiral vector theory unifies the steady-state AC circuit theory and transient-state theory, proving a powerful tool for analyzing the AC steady and transient states using the same state variables and notations. In addition, the spiral vector theory employs complex exponential phase variables and makes full use of the symmetry between phases to minimize the number of equations, further facilitating theoretical derivations.

The main contributions of this study are as follows.

(1) A spiral vector model for the unified steady-state and dynamic analysis of various BDFIMs with short-circuited rotor windings was been developed.

(2) Accurate finite element analysis assisted by the developed spiral vector model was conducted to show the torque characteristics of BDFIMs.

(3) The doubly-fed and singly-fed synchronous modes of BDFIM operation were analyzed based on the same spiral vector model.

(4) Theoretical performance comparison between a BDFIM and traditional non-salient-pole wound-field synchronous machine was presented for the first time.

(5) Prototyping of a 1.5-kW BDFIM and experimental validations were conducted.

The remainder of the paper is organized as follows. Section 2 introduces fundamentals of the investigated BDFIM system with short-circuited rotor windings. Section 3 presents the proposed unified spiral vector model. The parameter calculations are also discussed in this section. Section 4 reports on the performance analysis for steady-state operation, together with a comparison between the BDFIM and non-salient-pole wound-field synchronous machine. Section 5 describes the fabrication and experimental tests of a scaled-down prototype for validation. Section 6 concludes the paper.

2   Fundamentals of BDFIMs

A BDFIM typically has two distributed stator windings, referred to as stator windings 1 and 2 (SW1 and SW2, respectively) in this paper. It should be note

that although the two stator windings are usually configured to have 3 or more phases for doubly-fed synchronous operation, one of them can be a single-phase winding supplied by a DC current, in which case the machine can only be operated in the singly-fed synchronous mode.

A cross-sectional view of a typical 3-phase BDFIM is illustrated in Fig. 1a. The numbers of pole pairs of SW1 and SW2 are p_1=4 and p_2=2, respectively. The rotor has N_r=p_1+p_2=6 loop nests, and each nest has 3 concentric copper loops. The rotor winding can also be of spiral loop [29] or doubly-layer multiphase type with equal- or unequal-turn coils [10]. The coordinate system used to derive the spiral vector model of BDFIMs with short-circuited rotor windings is also illustrated in Fig. 1a. A nested-loop rotor is shown as an example. The two stator windings are supplied by two independent voltage sources for wider speed operation.

The system configuration with two independent converters is shown in Fig. 1b. The operating principle of the investigated BDFIM can be well explained by the airgap field modulation theory [30-31]. Once SW2 is energized by AC or DC current, a $2p_2$-pole magneto-motive force (MMF) is created in the airgap. When the rotor spins at a speed of ω_r, eddy currents are induced in nested rotor loops. The rotor MMF produced by the eddy currents has a series of harmonics rotating at different mechanical speeds, where those with $N_r-p_2=p_1$ poles have the largest amplitude. This MMF harmonic component can produce alternating flux linkages in SW1 and thus induce voltages.
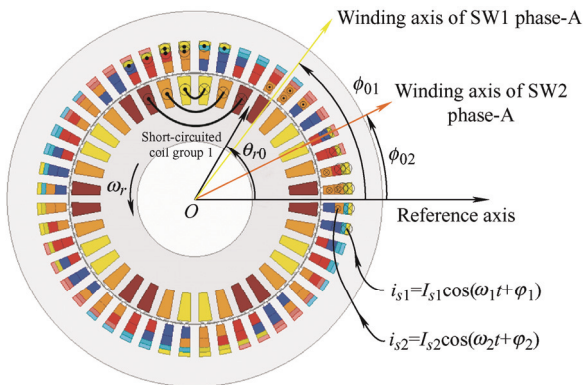
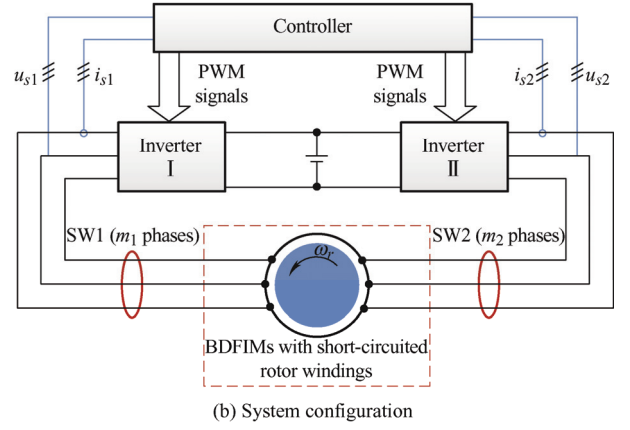(a) Cross-sectional view of a BDFIM

(b) System configuration

Fig. 1 A BDFIM in doubly-fed (or singly-fed) synchronous mode and its drive system

3 Modeling of BDFIM

In this section, the first concise mathematical model for BDFIMs using spiral vectors is presented to assist in performance evaluation using finite element analysis, which considers the initial phase of excitations, positions of winding axes, and the initial rotor position. This can be directly implemented for setting up finite element models.

It should be noted that all finite element simulations described in this paper are based on pure sinusoidal current or voltage excitations. In real-world applications, both stator windings will be supplied by voltage source inverters. Therefore, there will be some high-order harmonics in the current excitations, which will introduce additional losses and vibrations.

3.1 Spiral vectors

The spiral vector theory manipulates voltage and current as complex exponential variables to obtain a closed-form analytical solution for AC electrical circuits and machines [32]. Different from the complex vector notation presented in Ref. [33], the spiral vector theory treats each phase voltage and current as a complex exponential function of time [34].

In a steady state, the voltage and current spiral vectors are circular vectors and can be described as

$$\begin{cases} \boldsymbol{u}_{s1}(t) = U_{s1}\exp\left(j\left(\omega_1 t + \vartheta_1\right)\right) \\ \boldsymbol{u}_r(t) = 0 \\ \boldsymbol{u}_{s2}(t) = U_{s2}\exp\left(j\left(\omega_2 t + \vartheta_2\right)\right) \end{cases} \quad (1)$$

$$\begin{cases} \boldsymbol{i}_{s1}(t) = I_{s1}\exp\big(j(\omega_1 t + \varphi_1)\big) \\ \boldsymbol{i}_r(t) = I_r\exp\big(j\big[(\omega_1 - p_1\omega_r)t + \varphi_r\big]\big) \\ \boldsymbol{i}_{s2}(t) = I_{s2}\exp\big(j(\omega_2 t + \varphi_2)\big) \end{cases} \quad (2)$$

where $\boldsymbol{u}_{s1}$, $\boldsymbol{u}_r$, and $\boldsymbol{u}_{s2}$ are terminal voltage circular vectors of SW1, rotor loops, and SW2, respectively. U_{s1} and U_{s2} are the amplitudes of terminal voltages of SW1 and SW2, respectively. ω_1 and ω_2 are the electrical angular frequencies of SW1 and SW2, respectively. ϑ_1 and ϑ_2 are initial phase angles of terminal voltages of SW1 and SW2, respectively. $\boldsymbol{i}_{s1}$, $\boldsymbol{i}_r$, and $\boldsymbol{i}_{s2}$ are current circular vectors of SW1, rotor loops, and SW2, respectively. I_{s1} and I_{s2} are the current amplitudes of SW1 and SW2, respectively. φ_1, φ_r and φ_2 are initial phase angles of the currents of SW1, rotor loops and SW2, respectively.

The actual terminal voltage and current will be the real parts of the corresponding circular vectors

$$\begin{cases} u_{s1}(t) = \mathrm{Re}\big[\boldsymbol{u}_{s1}(t)\big] = U_{s1}\cos(\omega_1 t + \vartheta_1) \\ u_r(t) = \mathrm{Re}\big[\boldsymbol{u}_r(t)\big] = 0 \\ u_{s2}(t) = \mathrm{Re}\big[\boldsymbol{u}_{s2}(t)\big] = U_{s2}\cos(\omega_2 t + \vartheta_2) \end{cases} \quad (3)$$

$$\begin{cases} i_{s1}(t) = \mathrm{Re}\big[\boldsymbol{i}_{s1}(t)\big] = I_{s1}\cos(\omega_1 t + \varphi_1) \\ i_r(t) = \mathrm{Re}\big[\boldsymbol{i}_r(t)\big] = I_r\cos\big[(\omega_1 - p_1\omega_r)t + \varphi_r\big] \\ i_{s2}(t) = \mathrm{Re}\big[\boldsymbol{i}_{s2}(t)\big] = I_{s2}\cos(\omega_2 t + \varphi_2) \end{cases} \quad (4)$$

3.2 Unified spiral vector model

Based on the coordinate system defined in Fig. 1a, the voltage equation can be written concisely as

$$\boldsymbol{u} = \boldsymbol{z}\boldsymbol{i} \quad (5)$$

where the voltage vector, current vector, and impedance matrix are

$$\boldsymbol{u} = \Big[\ \boldsymbol{u}_{s1}\exp\big(jp_1\phi_{01}\big) \quad 0 \quad \big(\boldsymbol{u}_{s2}\exp\big(jp_2\phi_{02}\big)\big)^{*}\exp\big(jN_r\theta_r\big)\ \Big]^{\mathrm{T}} \quad (6)$$

$$\boldsymbol{i} = \Big[\ \boldsymbol{i}_{s1}\exp\big(jp_1\phi_{01}\big) \quad \boldsymbol{i}_r\exp\big(jp_1\theta_r\big) \quad \big(\boldsymbol{i}_{s2}\exp\big(jp_2\phi_{02}\big)\big)^{*}\exp\big(jN_r\theta_r\big)\ \Big]^{\mathrm{T}} \quad (7)$$

$$\boldsymbol{z} = \begin{bmatrix} r_{s1}+sL_{s1} & s\left(\dfrac{N_r}{2}\right)[\boldsymbol{L}_{s1r}] & 0 \\ s_1\left(\dfrac{m_1}{2}\right)[\boldsymbol{L}_{s1r}]^{\mathrm{T}} & [\boldsymbol{r}_r]+s_1\big([\boldsymbol{L}_r]-[\boldsymbol{L}_{r\text{-}r}]\big) & s_1\left(\dfrac{m_2}{2}\right)[\boldsymbol{L}_{s2r}]^{\mathrm{T}} \\ 0 & s_2\left(\dfrac{N_r}{2}\right)[\boldsymbol{L}_{s2r}] & r_{s2}+s_2L_{s2} \end{bmatrix} \quad (8)$$

with

$$\begin{cases} s_1 = s - jp_1\omega_r \\ s_2 = s - jN_r\omega_r \end{cases} \quad (9)$$

where r_{s1}, $\boldsymbol{r}_r$, and r_{s2} are the SW1 resistance, rotor resistance matrix, and SW2 resistance, respectively. L_{s1}, $\boldsymbol{L}_r$, and L_{s2} are the SW1 self-inductance, rotor self-inductance matrix, and SW2 self-inductance, respectively. $\boldsymbol{L}_{s1r}$, $\boldsymbol{L}_{r\text{-}r}$, and $\boldsymbol{L}_{s2r}$ are the SW1-rotor mutual inductance vector, mutual inductance matrix between any two rotor nests, and SW2-rotor mutual inductance vector, respectively. ϕ_{01} and ϕ_{02} are position angles of the SW1 and SW2 axes with respect to the reference axis, respectively. θ_r is the rotor position with respect to the reference axis. The dimensions of the rotor resistance matrix and rotor-related inductance matrices depend on the number of independent loops per nest.

The electromagnetic torque can be derived from the partial variation of co-energy with respect to position. Further, it can be represented in terms of the three current spiral (circular) vectors as

$$T_{em} = p_1\left(\frac{N_r}{2}\right)\left(\frac{m_1}{2}\right)\boldsymbol{L}_{s1r}\,\mathrm{Im}\Big[\big(\boldsymbol{i}_{s1}\exp\big(jp_1\phi_{01}\big)\big)\big(\boldsymbol{i}_r\exp\big(jp_1\theta_r\big)\big)^{*}\Big] +$$
$$p_2\left(\frac{N_r}{2}\right)\left(\frac{m_2}{2}\right)\boldsymbol{L}_{s2r}\,\mathrm{Im}\Big[\big(\boldsymbol{i}_{s2}\exp\big(jp_2\phi_{02}\big)\big)^{*}\exp\big(jN_r\theta_r\big)\big(-\boldsymbol{i}_r\exp\big(jp_1\theta_r\big)\big)^{*}\Big] \quad (10)$$

3.3 Parameter calculation

The parameters used in the spiral vector model can be calculated from the machine geometry based on the winding function theory, or finite element analysis for better accuracy. The inductance waveforms obtained from finite element analysis are illustrated in

Fig. 2 as an example. SW1 and SW2 have 8 and 4 poles, respectively. These inductances involve the closed rotor windings and cannot be measured directly through experimental tests. In the performance prediction based on finite element analysis, these inductances are naturally included in the model and require no additional estimations except the end

winding leakage inductances. The nonlinearity introduced by the magnetic saturation of laminated stator and rotor cores is considered naturally in the finite element analysis.

The self-inductances of SW1 and SW2 are DC values superimposed by some harmonic components introduced mainly by the winding spatial harmonics. The mutual inductances between stator windings and rotor nests are bipolar and dominated by the fundamental component, which is desired in the design of this type of BDFIM to suppress time and spatial harmonics.
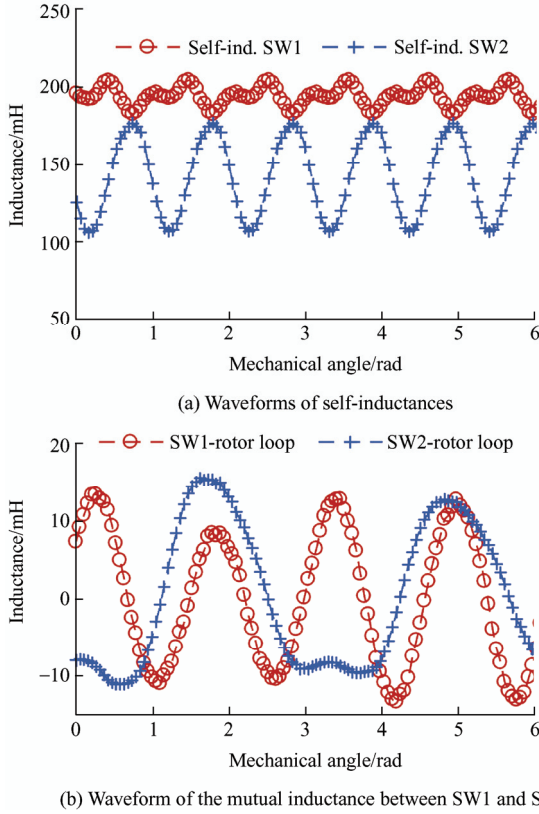

(a) Waveforms of self-inductances

(b) Waveform of the mutual inductance between SW1 and SW2

Fig. 2   Inductance waveforms obtained from finite element analysis of a BDFIM with spiral loop rotor windings

4   Steady-state operation

There are two types of synchronous BDFIM operation: doubly-fed and singly-fed, as mentioned in Section 2. In the doubly-fed synchronous mode of operation, both stator windings are supplied by AC voltages or currents, and the rotor speed meets the frequency constraint

$$\omega_r = \frac{\omega_1 + \omega_2}{p_1 + p_2} \quad \omega_1, \ \omega_2 \neq 0 \tag{11}$$

Therefore, the rotor slip frequency is

$$\omega_{s1} = \omega_1 - p_1 \omega_r = \frac{\omega_1 p_2 - p_1 \omega_2}{p_1 + p_2} \quad \omega_1, \ \omega_2 \neq 0 \tag{12}$$

and the SW2 slip frequency is

$$\omega_{s2} = \omega_1 - (p_1 + p_2)\omega_r = -\omega_2 \quad \omega_1, \ \omega_2 \neq 0 \tag{13}$$

In the singly-fed synchronous mode of operation, one of the stator windings is supplied by a DC voltage or current. Assuming SW1 is supplied by an AC source and SW2 by a DC source, the rotor speed will be

$$\omega_r = \frac{\omega_1}{p_1 + p_2} \quad \omega_2 = 0 \tag{14}$$

The SW2 slip frequency is zero, and the rotor slip frequency is

$$\omega_{s1} = \omega_1 - p_1 \omega_r = \frac{p_2}{p_1 + p_2}\omega_1 \quad \omega_2 = 0 \tag{15}$$

4.1   Doubly-fed synchronous operation

In a steady state, the differential operator s is replaced by $j\omega_1$, and Eqs. (6)-(8) can be simplified to

$$\boldsymbol{U} = \left[U_{s1}\exp(j\vartheta_1)\exp(jp_1\phi_{01}) \quad 0 \quad \left(U_{s2}\exp(j\vartheta_2)\exp(jp_2\phi_{02}) \right)^* \exp(jN_r\theta_{r0}) \right]^{\mathrm{T}} \tag{16}$$

$$\boldsymbol{I} = \left[I_{s1}\exp(j\varphi_1)\exp(jp_1\phi_{01}) \quad I_r\exp(j\varphi_r)\exp(jp_1\theta_{r0}) \quad \left(I_{s2}\exp(j\varphi_2)\exp(jp_2\phi_{02}) \right)^* \exp(jN_r\theta_{r0}) \right]^{\mathrm{T}} \tag{17}$$

$$\boldsymbol{Z} = \begin{bmatrix} r_{s1} + j\omega_1 L_{s1} & j\omega_1\left(\dfrac{N_r}{2}\right)\boldsymbol{L}_{s1r} & 0 \\[2ex] j\omega_{s1}\left(\dfrac{m_1}{2}\right)\boldsymbol{L}_{s1r}^{\mathrm{T}} & r_r + j\omega_{s1}\left(\boldsymbol{L}_r - \boldsymbol{L}_{r-r}\right) & j\omega_{s1}\left(\dfrac{m_2}{2}\right)\boldsymbol{L}_{s2r}^{\mathrm{T}} \\[2ex] 0 & j\omega_{s2}\left(\dfrac{N_r}{2}\right)\boldsymbol{L}_{s2r} & r_{s2} + j\omega_{s2}L_{s2} \end{bmatrix} \tag{18}$$

The electromagnetic torque will be

$$T_{em} = p_1 \left(\frac{N_r}{2} \right) \left(\frac{m_1}{2} \right) \boldsymbol{L}_{s1r} \times \mathrm{Im} \left[\left(I_{s1} \exp(j\varphi_1) \exp(jp_1\phi_{01}) \right) \left(I_r \exp(j\varphi_r) \exp(jp_1\theta_{r0}) \right)^* \right] +$$

$$p_2 \left(\frac{N_r}{2} \right) \left(\frac{m_2}{2} \right) \boldsymbol{L}_{s2r} \times \mathrm{Im} \left[\left(I_{s2} \exp(j\varphi_2) \exp(jp_2\phi_{02}) \right)^* \exp(jN_r\theta_{r0}) \left(-I_r \exp(j\varphi_r) \exp(jp_1\theta_{r0}) \right)^* \right] \quad (19)$$

The spiral vector diagram of the voltage in Eqs. (16)-(18) can be drawn in a similar manner to those for conventional induction machines, as shown in Fig. 3.
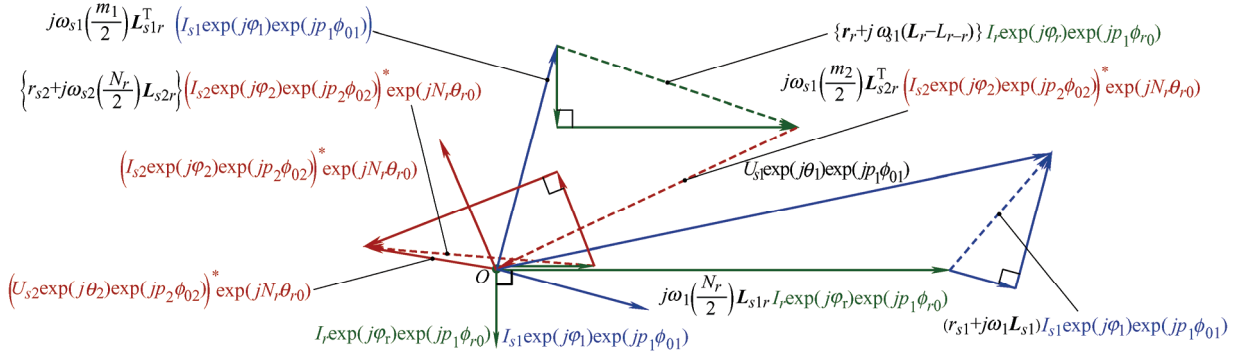

Fig. 3   Spiral vector diagram of BDFIM with short-circuited rotor windings

By using the proposed spiral vector theory-based modeling approach, a vector diagram similar to the traditional phasor diagram can be easily obtained based on Eqs. (16)-(18), allowing visualization of the amplitudes and phases of voltages and currents. The complex conjugates of the SW2 voltage and current vectors are introduced due to the fact that the rotating magnetic fields of the 2p1-and 2p2-pole are in opposite directions relative to the rotor.

The rotor current vector can be obtained from Eq. (18) as follows

$$I_r \exp(j\varphi_r) \exp(jp_1\theta_{r0}) = -\left\{ \boldsymbol{r}_r + j\omega_{s1}(\boldsymbol{L}_r - \boldsymbol{L}_{r-r}) \right\}^{-1} \times$$

$$\left\{ \left(I_{s1} \exp(j\varphi_1) \exp(jp_1\phi_{01}) \right) j\omega_{s1} \left(\frac{m_1}{2} \right) \boldsymbol{L}_{s1r}^\mathrm{T} + \right.$$

$$\left. \left[\left(I_{s2} \exp(j\varphi_2) \exp(jp_2\phi_{02}) \right)^* \exp(jN_r\theta_{r0}) \right] j\omega_{s1} \left(\frac{m_2}{2} \right) \boldsymbol{L}_{s2r}^\mathrm{T} \right\} \quad (20)$$

By neglecting the rotor resistance matrix, which can usually be done for well-designed BDFIMs, the rotor current can be simplified to

$$I_r \exp(j\varphi_r) \exp(jp_1\theta_{r0}) = -\left\{ (\boldsymbol{L}_r - \boldsymbol{L}_{r-r}) \right\}^{-1} \times$$

$$\left\{ \left(I_{s1} \exp(j\varphi_1) \exp(jp_1\phi_{01}) \right) \left(\frac{m_1}{2} \right) \boldsymbol{L}_{s1r}^\mathrm{T} + \right.$$

$$\left. \left[\left(I_{s2} \exp(j\varphi_2) \exp(jp_2\phi_{02}) \right)^* \exp(jN_r\theta_{r0}) \right] \left(\frac{m_2}{2} \right) \boldsymbol{L}_{s2r}^\mathrm{T} \right\} \quad (21)$$

Then, the torque equation can be simplified to

$$T_{em} = (p_1 + p_2) L_{1r2} I_{s1} I_{s2} \sin\gamma \quad (22)$$

where L_{1r2} is the mutual inductance between SW1 and SW2 through the intermediate action of the rotor with short-circuited windings, which can be expressed by

$$L_{1r2} = \left(\frac{N_r}{2} \right) \left(\frac{m_1}{2} \right) \boldsymbol{L}_{s1r} \left(\boldsymbol{L}_r - \boldsymbol{L}_{r-r} \right)^{-1} \left(\frac{m_2}{2} \right) \boldsymbol{L}_{s2r}^\mathrm{T} \quad (23)$$

and

$$\gamma = (p_1\phi_{01} + \varphi_1) + (p_2\phi_{02} + \varphi_2) - N_r\theta_{r0} \quad (24)$$

where γ is the current angle.

Eq. (22) indicates that the torque of a BDFIM with short-circuited rotor windings is proportional to the amplitudes of the SW1 and SW2 currents, and the torque angle. The torque angle not only depends on the initial phase angles of the SW1 and SW2 currents, but also the positions of winding axes of SW1 and SW2, and the initial rotor position, when the rotor resistance can be neglected.

The spiral vector diagram shown in Fig. 3 can be further simplified to illustrate the torque production due to the SW1 and SW2 currents, as

shown in Fig. 4. The rotor winding resistance, stator winding resistances, and leakage inductances are neglected for simplified analysis, which is a common practice in analyzing AC synchronous machines. The upper and lower triangles represent the voltage and current relations of SW2 and SW1, respectively. By applying the law of sines, more insights into the SW1- and SW2-related quantities can be obtained. The area of the parallelogram is proportional to the torque.
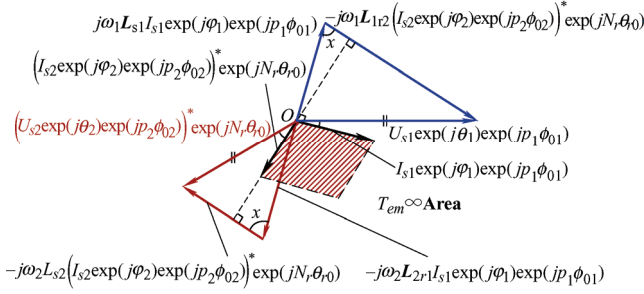
Fig. 4 Simplified spiral vector diagram of BDFIM with short-circuited rotor windings

This conclusion can be directly implemented in finite element analysis to determine the torque-angle characteristics, and the maximum torque occurs around $\gamma=\pm\pi/2$, as illustrated in Fig. 5, where "TR" stands for transient solver and "QS" stands for quasi-static solver. Without the developed spiral vector model, the zero-crossing point and peak torque points will be randomly positioned. It can also be seen that with a smaller rotor resistance, the peak torque will be larger. Regardless of the rotor resistance, torque-angle curves from the transient solver will be distorted, but curves from the quasi-static solver will always be symmetrical.

The flux pattern will vary with changes in the current ratios, i.e., I_{s1}/I_{s2}, leading to different levels of saturation in the stator and rotor back irons, as shown in Fig. 6, where F_1 and F_2 represent the per-pole MMF of SW1 and SW2, respectively, which depend on the stator currents. When the per-pole MMFs of SW1 and SW2 are the same, the flux contour shows a (p_1+p_2)-pole pattern. By contrast, when the per-pole

MMF of SW2 is larger, the flux contour will be dominated by the $2p_2$-pole pattern.
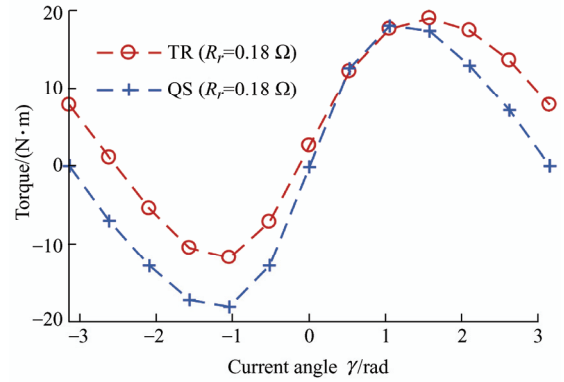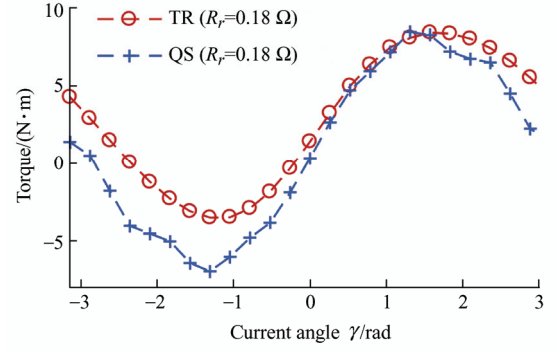
(a) Considering the rotor resistance

(b) Neglecting the rotor resistance

Fig. 5 Finite element analysis predicted torque-current angle curves

(a) Flux lines   (b) Flux density distribution
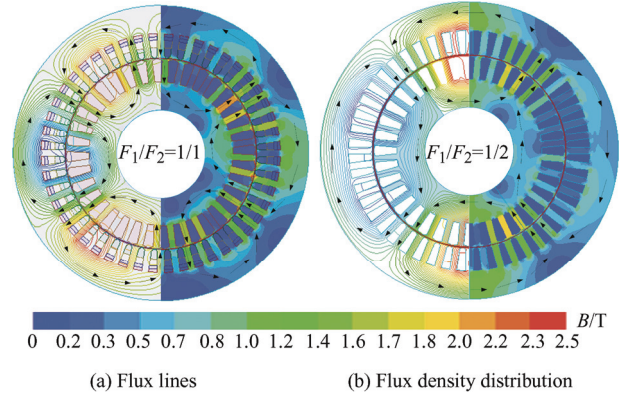
Fig. 6 Field plots of the BDFIM

4.2 Singly-fed synchronous operation

In the singly-fed synchronous mode of operation, SW2 is supplied by a DC current, and the previously introduced equations can be simplified to

$$\boldsymbol{U} = \left[U_{s1}\exp\left(j\varphi_1\right)\exp\left(jp_1\phi_{01}\right) \quad 0 \quad \left(U_{s2}\exp\left(jp_2\phi_{02}\right)\right)^{*}\exp\left(jN_r\theta_{r0}\right) \right]^{\mathrm{T}} \tag{25}$$

$$\boldsymbol{I} = \left[I_{s1}\exp\left(j\varphi_1\right)\exp\left(jp_1\phi_{01}\right) \quad I_r\exp\left(j\varphi_r\right)\exp\left(jp_1\theta_{r0}\right) \quad \left(I_{s2}\exp\left(jp_2\phi_{02}\right)\right)^{*}\exp\left(jN_r\theta_{r0}\right) \right]^{\mathrm{T}} \quad (26)$$

$$\boldsymbol{Z} =$$

$$\begin{bmatrix} r_{s1}+sL_{s1} & j\omega_1\left(\dfrac{N_r}{2}\right)\boldsymbol{L}_{s1r} & 0 \\[2em] j\omega_{s1}\left(\dfrac{m_1}{2}\right)\boldsymbol{L}_{s1r}^{\mathrm{T}} & \boldsymbol{r}_r+j\omega_{s1}\left(\boldsymbol{L}_r-\boldsymbol{L}_{r-r}\right) & j\omega_{s1}\left(\dfrac{m_2}{2}\right)\boldsymbol{L}_{s2r}^{\mathrm{T}} \\[2em] 0 & 0 & r_{s2} \end{bmatrix}$$
$$(27)$$

The torque equation is the same as Eq. (22). Rewriting Eq. (22) using the no-load flux linkage produced by SW2, the torque will be

$$T_{em} = \left(p_1+p_2\right)\psi_{s2}I_{s1}\sin\gamma \quad (28)$$

where

$$\psi_{s2} = L_{1r2}I_{s2} \quad (29)$$

The active power delivered by SW1 can be calculated by multiplying Eq. (28) by the rotor speed

$$P = \omega_1\psi_{s2}I_{s1}\sin\gamma \quad (30)$$

Rewriting Eq. (30) with voltages instead of currents, the power equation becomes similar to that of a traditional wound-field non-salient-pole synchronous machine is obtained as

$$P = \frac{E_0 U_{s1}}{X_s}\sin\delta \quad (31)$$

where $E_0=\omega_1\psi_{s2}$ is the no-load voltage, δ is the power angle, $X_s=(m_1/2)\omega_1 C_{12}L_{ms1}$ is the synchronous reactance, and L_{ms1} is the main self-inductance of SW1 without considering the influence of rotor loops. C_{12} is the conversion factor introduced by the rotor loops, which can be expressed by

$$C_{12} = 1 - \left(\frac{1}{L_{ms1}}\right)\left(\frac{N_r}{2}\right)\boldsymbol{L}_{s1r}\left(\boldsymbol{L}_r-\boldsymbol{L}_{r-r}\right)^{-1}\left(\frac{m_2}{2}\right)\boldsymbol{L}_{s2r}^{\mathrm{T}} \quad (32)$$

Eq. (31) indicates that a BDFIM with short-circuited rotor windings operated in singly-fed synchronous mode is equivalent to a wound-field non-salient-pole synchronous machine. Its no-load terminal voltage is proportional to the frequency of stator currents and the flux linkage produced by the SW2. The synchronous reactance can be calculated from the conversion factor and the SW1 main inductance.

The synchronous reactance is reduced due to the presence of the short-circuited rotor windings because C_{12} is theoretically always below 1.0. The simplified phasor diagram used for steady-state analysis of the BDFIM in singly-fed synchronous mode is shown in Fig. 7.
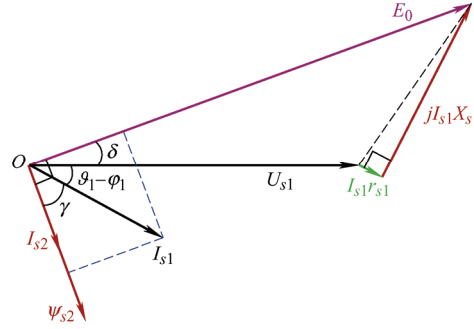

Fig. 7   Simplified phasor diagram

4.3 Comparison with synchronous machine

A comparison between the BDFIM with short-circuited rotor windings and a wound-field synchronous machine of the same geometry is made here in terms of the per-phase flux linkage linked by SW1, the back-electromotive force (back-EMF), and torque per rotor volume. The ratios of flux linkage (back-EMF, torque per rotor volume) between the BDFIM and synchronous machine are tabulated in Tab. 1.

Tab. 1   Comparison of BDFIM and synchronous machine

Equal per-pole excitation MMF (*PF* is the power factor of SW1)		
Ratio of per phase flux linkage	Ratio of back-EMF at the same rotor speed	Ratio of torque per rotor volume
C_{12}	$C_{12}\left(\dfrac{p_1+p_2}{p_1}\right)$	$C_{12}\left(\dfrac{p_1+p_2}{p_1}\right)\dfrac{PF_{BDFIM}}{PF_{SM}}$
Equal overall excitation MMF (*PF* is the power factor of SW1)		
Ratio of per phase flux linkage	Ratio of back-EMF at the same rotor speed	Ratio of torque per rotor volume
$C_{12}\left(\dfrac{p_1}{p_2}\right)$	$C_{12}\left(\dfrac{p_1+p_2}{p_2}\right)$	$C_{12}\left(\dfrac{p_1+p_2}{p_2}\right)\dfrac{PF_{BDFIM}}{PF_{SM}}$

To produce the same flux linkage in SW1, the overall SW2 MMF of the BDFIM should be $p_2/(C_{12}\times p_1)$ times that of the synchronous machine. For the investigated topology (p_1=4, p_2=2, C_{12} calculated from finite element model=0.495 8, C_{12} calculated

from analytical method=0.439 6), the consumed total excitation MMF is nearly the same. If the saturation effect is further taken into consideration, the flux linkage ratio drops after the laminated core becomes saturated, as illustrated in Fig. 8.
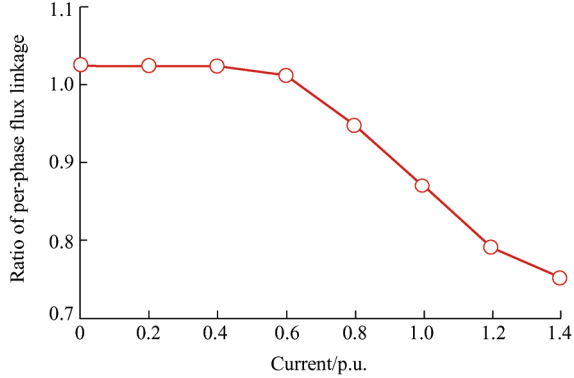

Fig. 8   Flux linkage ratios at different saturation levels

It can be concluded that in unsaturated and low-saturated operating conditions, the investigated BDFIM can achieve nearly the same torque as a traditional non-salient-pole synchronous machine with the same rotor volume and overall MMFs. However, the excitation becomes ineffective when the stator and/or rotor cores are heavily saturated. The overall capability is relatively weak compared with the traditional wound-field synchronous machine.

5   Prototyping and experimental validation

A scaled-down BDFIM prototype with spiral-loop rotor windings and a slip-ring doubly-fed induction machine operated as a wound-field synchronous machine were used to validate the effectiveness of the developed model and correctness of the theoretical analysis.

The two prototypes are shown in Figs. 9 and 10, respectively. Their specifications are listed in Tab. 2. A spiral loop rotor was adopted instead of a nested-loop one to simplify the fabrication of the rotor winding. A spiral loop rotor is expected to have similar characteristics to its nested-loop counterpart, except the increased rotor resistance. Phase A and phase B of the 3-phase SW2 were connected in parallel and then connected in series with phase C to form an equivalent DC winding in singly-fed synchronous mode. The SW1 winding served as the AC winding.
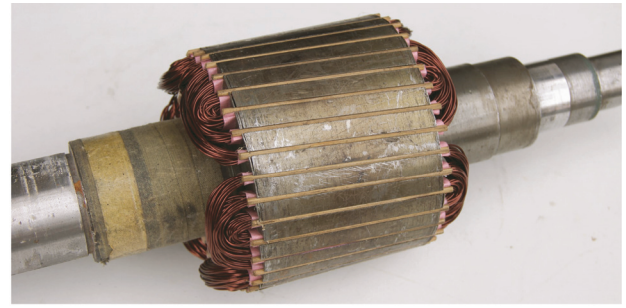
(a) Rotor
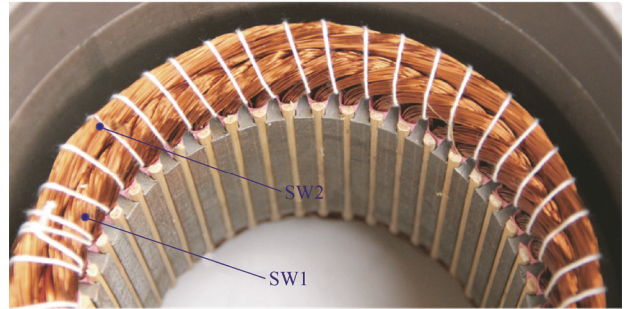
(b) Stator in the frame

Fig. 9   Photos of the 1.5-kW BDFIM

(a) Rotor

(b) Stator in the frame

Fig. 10   Photos of the 1.5-kW wound-field synchronous machine (doubly-fed induction machine with the rotor winding supplied by DC currents)
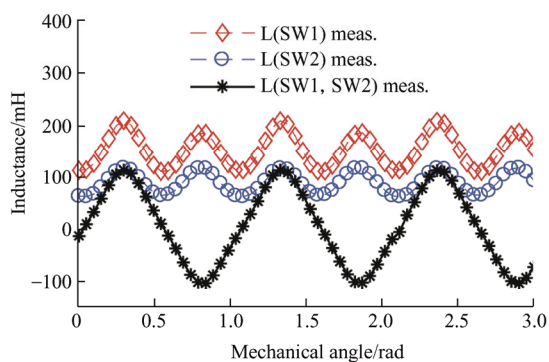
Tab. 2   Ratings and specifications of the 1.5-kW prototype

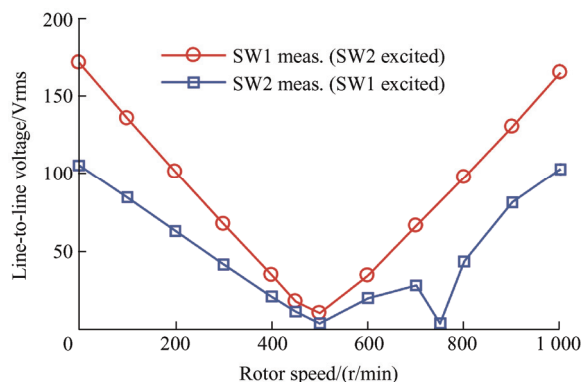| Parameter	Value
Rated power/kW	1.5
Maximum torque/(N·m), speed/(r/min)	21, 4 000
Stator outer/mm, inner diameter/mm	182, 127
Air gap/mm, stack length/mm	0.35, 90
Stator/rotor slot number	45/36
Number of spiral loops	6
Turns per spiral loop	15
Rotor slot skewing angle /(°)	8
Turns in series per phase of 8-pole winding (3-phase)	510
Turns in series per phase of 4-pole winding (3-phase)	255
Mechanical angle between phase A axes of SW1 and SW2/(°)	0

The unsaturated inductances were measured at different rotor positions with an LCR meter at 50 Hz, which is the rated frequency at the designed operating point. In addition, because the rotor is stationary, a 50 Hz excitation to SW1 and SW2 can provide a relatively large slip frequency to reduce the influence of the rotor winding resistance. To test the inductances, the SW1 terminals were reconnected in a similar manner to the SW2 ones because the three phases were star-connected and there was no accessible neutral point. Phase A and phase B of SW1 were connected in parallel and then connected in series with phase C. The tested inductance waveforms are shown in Fig. 11a.

The self-inductances of SW1 and SW2 are DC values superimposed by some harmonic components. The mutual inductance between SW1 and SW2 is rotor position-dependent and varies sinusoidally when the rotor spins at a constant speed. Based on the analysis presented in Section 4, the mutual inductance between SW1 and SW2 can be measured and used to characterize the machine without knowing the detailed mutual inductances between stator windings and rotor loops, which cannot be measured directly in reality because the rotor windings are closed. This feature enables performance comparison between BDFIMs, CDFIMs, and BDFRMs.
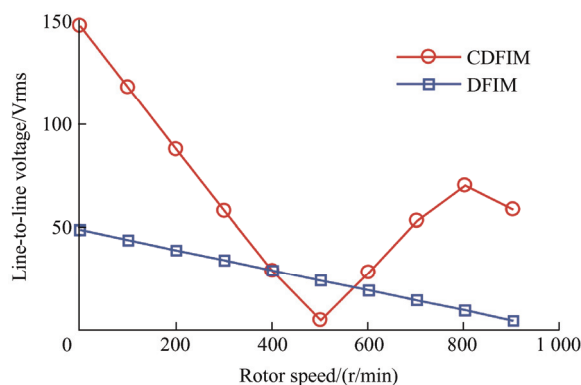
The measured open-circuit terminal voltages at different speeds, which are a good measure of the cross-coupling capability in voltage mode [35], for the BDFIM prototype, slip-ring doubly-fed induction machine, and cascade of two doubly-fed induction machines, i.e., the CDFIM, are shown in Fig. 11b and Fig. 11c.

(b) Open-circuit voltage for BDFIM

(c) Open-circuit voltage for CDFIM and
slip-ring doubly-fed induction machine

Fig. 11   Test results of the scaled-down prototype

In the test, both stator windings were used as 3-phase windings. One of the stator windings was supplied by a 50-Hz sinusoidal voltage source, and the open-circuit line-to-line voltage of the other stator winding was measured at different rotor speeds. When SW2 was energized by the 50-Hz current, the synchronous speed of SW2 was 1 500 r/min, making the induced voltage in SW1 vary linearly. On the contrary, when SW1 was energized by the 50-Hz current, the synchronous speed became 750 r/min. As the rotor speed approached 750 r/min, the slip frequency became zero and there was no current in the spiral loops. Therefore, the measured line-to-line voltage at 750 r/min was close to zero. Similarly, the groove was also observed in the CDFIM, but at a different speed. This groove did not exist in the slip-ring doubly-fed induction machine.

To test the torque-angle curve, both stator windings were used as 3-phase windings and supplied by 50-Hz voltage sources. The phase sequence of one of the stator windings must be reversed so that the rotor speed can remain at zero. Then, the torque could be recorded at different rotor positions. At least a

(a) Inductance waveforms considering the influence
of short-circuited rotor windings

range of 60 deg. (mechanical) was required to obtain the full torque-angle curve.

6 Conclusions

A BDFIM with short-circuited rotor windings was modeled using spiral vectors, based on which finite element analysis was conducted to analyze its performance. It was found that a BDFIM in singly-fed synchronous mode is equivalent to a wound-field non-salient-pole synchronous machine in terms of torque/power-angle characteristics. Its performance can be analyzed with methods similar to those of conventional phasor theory, after the conversion factor is introduced.

In unsaturated and low-saturated operating conditions, the investigated BDFIM can achieve nearly the same torque as a traditional non-salient-pole synchronous machine with the same rotor volume and overall MMFs. However, the excitation becomes ineffective when the iron core is heavily saturated. The overall capability is relatively weak compared with that of the traditional wound-field synchronous machine. A more detailed comparison of BDFIMs, CDFIMs, and BDFRMs based on unified spiral vector models is underway and will be reported in the future.

References

[1] M Cheng, Y Zhu. The state of the art of wind energy conversion systems and technologies: A review. *Energy Convers. Manage.*, 2014, 88: 332-347.

[2] L Xu, Y Liu, X Wen. Comparison study of singly-fed electric machine with doubly-fed machine for EV/HEV applications. *in Proc. Int. Conf. Electr. Mach. Syst.* (*ICEMS*), Beijing, China, 20-23 Aug. 2011.

[3] R A McMahon, P C Roberts, X Wang, et al. Performance of BDFM as generator and motor. *IEE Proc.-Electr. Power Appl.*, 2006, 153(2): 289-299.

[4] P Han, M Cheng, Z Chen. Dual-electrical-port control of cascaded doubly-fed induction machine for EV/HEV applications. *IEEE Trans. Ind. Appl.*, 2017, 53(2): 1390-1398.

[5] R S Rebeiro, A M Knight. Two-converters-based synchronous operation and control of a brushless doubly fed reluctance machine. *IEEE Trans. Mag.*, 2018, 54(11): 8107205.

[6] Z Zhang. Robust stator-excited brushless synchronous machine: An attractive permanent magnet-free option. *in Proc. Int. Conf. Electr. Mach. Syst.* (*ICEMS*), Harbin, China, 11-14 Aug. 2019.

[7] Z Zhang. A brushless doubly fed machine with separated field and armature windings in dual stators. *in Proc. Int. Electr. Mach. Drives Conf. (IEMDC)*, San Diego, CA, USA, 12-15 May, 2019.

[8] P Han, M Cheng, S Ademi, et al. Brushless doubly-fed machines: Opportunities and challenges. *Ch. J. Electr. Eng.*, 2018. 4(2): 1-17.

[9] M Ruviaro, F Runcos, N Sadowski, et al. Analysis and test results of a brushless doubly fed induction machine with rotary transformer. *IEEE Tran. Ind. Electron.* 2011, 59(6): 2670-2677.

[10] F Xiong, X Wang. Design of a low-harmonic-content wound rotor for the brushless doubly fed generator. *IEEE Trans. Energy Convers.*, 2014, 29(1): 158-168.

[11] F Zhang, S Yu, X Wang, et al. Research of a novel brushless doubly-fed generator with hybrid rotor. *IEEE Trans. Appl. Supercond.*, 2016, 26(7): 0608205.

[12] R Li, A Wallace, R Spée. Dynamic modeling, simulation and stability analysis of brushless doubly-fed machines. *IEEE Trans. Energy Convers.*, 1991, 6(3): 445-452.

[13] R Li, A K Wallace, R Spée. Two-axis model development of cage rotor brushless doubly-fed machines. *IEEE Trans. Energy Convers.*, 1991, 6(3): 453-460.

[14] R Li, A K Wallace, G C Alexander. Dynamic simulation of brushless doubly-fed machines. *IEEE Trans. Energy Convers.*, 1991, 6(3): 445-452.

[15] J Poza, E Oarbide, D Roye, et al. Stability analysis of a BDFM under open-loop voltage control. *in Proc. European Conference on Power Electronics and Applications*, Dresden, Germany, Sep. 2005: 1-10.

[16] I Sarasola, J Poza, E Oyarbide, et al. Stability analysis of a brushless doubly-fed machine under closed loop scalar current control. *in Proc. Industrial Electronics Conference* (*IECON*), Paris, France, Nov. 2006: 1527-1532.

[17] P C Roberts, T J Flack, J M Maciejowski, et al. Two stabilizing control strategies for the brushless doubly-fed machine (BDFM). *in Proc. International Power Electronics, Machines and Drives Conference* (*IPEMDC*), Venue, UK, Jun. 2002: 341-346.

[18] D Zhou, R Spee, G C Alexander. Experimental evaluation of a rotor flux oriented control algorithm for brushless doubly-fed machines. *IEEE Trans. Power Electron.*, 1997, 12(1): 72-78.

[19] M S Boger, A K Wallace, R Spee, et al. General pole number model of the cage-rotor brushless doubly-fed machine. *IEEE Trans. Ind. Appl.*, 1995, 31(5): 1022-1028.

[20] P C Roberts, T Long, R A McMahon, et al. Dynamic modelling of the brushless doubly fed machine. *IET Proc.-Electr. Power Appl.*, 2013, 7(7): 544-556.

[21] J Poza, E Oyarbide, D Roye, et al. Unified reference frame d-q model of the brushless doubly-fed machine. *IET Proc.-Electr. Power Appl.*, 2006, 153(5): 726-734.

[22] J Poza, E Oyarbide, I Sarasola, et al. Vector control design and experimental evaluation for the brushless doubly fed machine. *IET Proc.-Electr. Power Appl.*, 2009, 3(4): 247-256.

[23] S Shao, E Abdi, F Barati, et al. Stator-flux-oriented vector control for brushless doubly fed induction generator. *IEEE Trans. Ind. Electron.*, 2009, 56(10): 4220-4228.

[24] F Barati, S Shao, E Abdi, et al. Generalized vector model for the brushless doubly-fed machine with a nested-loop rotor. *IEEE Trans. Ind. Electron.*, 2011, 58(6): 2313-2321.

[25] W R Brassfield, R Spee, T G Habetler. Direct torque control for brushless doubly-fed machines. *IEEE Trans. Ind. Appl.*, 1996, 32(5): 4474360.

[26] I Sarasola, J Poza, M A Rodriguez, et al. Direct torque control design and experimental evaluation for the brushless doubly fed machine. *Energy Convers. and Manage.*, 2011, 52(2): 1226-1234.

[27] A Zhang, X Wang, W Jia, et al. Indirect stator-quantities control for the brushless doubly fed induction machine. *IEEE Trans. Power Electron.*, 2014, 29(3): 1392-1401.

[28] R Zhao, A Zhang, Y Ma, et al. The dynamic control of reactive power for the brushless doubly fed induction machine with indirect stator-quantities control scheme. *IEEE Trans. Power Electron.*, 2015, 30(9): 5046-5057.

[29] H Gorginpour, B Jandaghi, H Oraee, et al. A novel rotor configuration for brushless doubly-fed induction generators. *IET Electr. Power Appl.*, 2013, 7(2): 106-115.

[30] M Cheng, P Han, W Hua. General airgap field modulation theory for electrical machines. *IEEE Trans. Ind. Electron.*, 2017, 64(8): 6063-6074.

[31] M Cheng, P Han, Y Du, et al. A tutorial on general air-gap field modulation theory for electric machines. *IEEE J. Emerg. Sel. Top. Power Electron.*, DOI: 10.1109/JESTPE. 2021.3055224.

[32] S Yamamura. Spiral vector theory of AC circuits and machine, 1st ed. Oxford: Clarendon, 1992.

[33] D W Novotny, T A Lipo. Complex vector analysis of induction machines. Vector control and dynamics of ac drives, 1st ed. New York: Oxford University Press Inc., 1996.

[34] P Han, M Cheng, X Wei, et al. Modeling and performance analysis of a dual-stator brushless doubly fed induction machine based on spiral vector theory. *IEEE Trans. Ind. Appl.*, 2016, 52(2): 1380-1389.

[35] P Han, M Cheng, X Wei, et al. Steady-state characteristics of the dual-stator brushless doubly fed induction generator. *IEEE Trans. Ind. Electron.*, 2018, 65(1): 200-210.

Peng Han received the B.Sc. and Ph.D. degrees in Electrical Engineering from the School of Electrical Engineering, Southeast University, Nanjing, China, in 2012 and 2017, respectively.

From November 2014 to November 2015, he was a joint Ph.D. student funded by China Scholarship Council with the Department of Energy Technology, Aalborg University, Aalborg, Denmark, where he focused on the brushless doubly-fed machines for wind energy conversion and high power drive. He was a Postdoctoral Researcher with the Center for High Performance Power Electronics (CHPPE), Department of Electrical and Computer Engineering, The Ohio State University, and later the SPARK Laboratory, Department of Electrical and Computer Engineering, University of Kentucky. He is currently with Ansys, Inc. as an Application Engineer. His current research interests include electric machines, power electronics and renewable energy.

Ming Cheng received the B.Sc. and M.Sc. degrees from the department of Electrical Engineering, Southeast University, Nanjing, China, in 1982 and 1987, respectively, and the Ph.D. degree from the Department of Electrical and Electronic Engineering, University of Hong Kong, Hong Kong, China, in 2001, all in Electrical Engineering.

Since 1987, he has been with Southeast University, where he is currently a Chief Professor at the School of Electrical Engineering and the Director of the Research Center for Wind Power Generation. From January to April 2011, he was a Visiting Professor with the Wisconsin Electric Machine and Power Electronics Consortium (WEMPEC), University of Wisconsin, Madison, WI, USA. His teaching and research interests include electrical machines, motor drives for EV, and renewable energy generation. He has authored or co-authored more than 400 technical papers and 5 books, and is the holder of 130 patents in these areas.

Prof. Cheng is a Fellow of the Institution of Engineering and Technology. He has served as the Chair and an Organizing Committee Member for many international conferences. He is a distinguished Lecturer of the IEEE Industry Application Society in 2015/2016.

Zhiwei Zhang received the Ph.D. degree in Electrical Engineering from the Huazhong University of Science and Technology, Wuhan, China, in 2016.

He is currently a Visiting Scholar with the Department of Electrical and Computer Engineering, The Ohio State University, Columbus, OH, USA. His current research interests include design and analysis of advanced electric machines, variable-speed ac drives, transportation electrification, and renewable energy conversion systems.
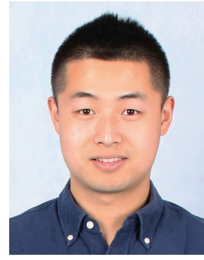
Peng Peng received the Ph.D. degree in Electrical and Computer Engineering from The Ohio State University, Columbus, OH, USA, in 2020.

Since 2021, he has been a Motor Control Engineer with Milwaukee Electric Tool Corporation developing control algorithms for high-speed motors. His research interests include electric machines, magnetic materials, control theory, and power electronics.